

# In vivo microstructural and microvascular imaging of the human corneo-scleral limbus using optical coherence tomography

Peng Li,<sup>1</sup> Lin An,<sup>1</sup> Roberto Reif,<sup>1</sup> Tueng T. Shen,<sup>1,2</sup> Murray Johnstone,<sup>2</sup> and Ruikang K Wang<sup>1,2,\*</sup>

<sup>1</sup>Department of Bioengineering, University of Washington, Seattle, Washington 98195, USA

<sup>2</sup>Department of Ophthalmology, University of Washington, Seattle, Washington 98195, USA

\*wangrk@uw.edu

**Abstract:** The corneo-scleral limbus contains several biological components, which are important constituents for understanding, diagnosing and managing several ocular pathologies, such as glaucoma and corneal abnormalities. An anterior segment optical coherence tomography (AS-OCT) system integrated with optical microangiography (OMAG) is used in this study to non-invasively visualize the three-dimensional microstructural and microvascular properties of the limbal region. Advantages include first the ability to correct optical distortion of microstructural images enabling quantification of relationships in the anterior chamber angle. Second, microvascular images enable the visualization of the microcirculation in the limbal area without the use of exogenous contrast agents. Third, by combining the microstructural and microvascular information, the aqueous outflow pathway can be identified. The proposed AS-OCT can serve as a useful tool for ophthalmological research to determine normal and pathologic changes in the outflow system. As a clinical tool it has the potential to detect early aqueous outflow system abnormalities that lead to the pressure elevation in glaucoma. Recent surgical innovations and their implementations also rely on an assessment of outflow system structure and function, which can be revealed by AS-OCT.

© 2011 Optical Society of America

**OCIS codes:** (170.4500) Optical coherence tomography; (170.0110) Imaging systems; (170.3880) Medical and biological imaging; (170.4470) Ophthalmology

## References and links

1. M. J. Hogan, J. A. Alvarado, and J. E. Weddell, *Histology of the Human Eye; an Atlas and Textbook* (Saunders, 1971), pp. xiii.
2. E. B. Papas, "The limbal vasculature," *Cont. Lens Anterior Eye* **26**(2), 71–76 (2003).
3. Y. Hayashi, M. K. Call, C. Y. Liu, M. Hayashi, G. Babcock, Y. Ohashi, and W. W. Kao, "Monoallelic expression of Krt12 gene during corneal-type epithelium differentiation of limbal stem cells," *Invest. Ophthalmol. Vis. Sci.* **51**(9), 4562–4568 (2010).
4. H. S. Dua and A. Azuara-Blanco, "Limbal stem cells of the corneal epithelium," *Surv. Ophthalmol.* **44**(5), 415–425 (2000).
5. M. F. Goldberg and A. J. Bron, "Limbal palisades of Vogt," *Trans. Am. Ophthalmol. Soc.* **80**, 155–171 (1982).
6. M. Johnstone, E. Martin, and A. Jamil, "Pulsatile flow into the aqueous veins: manifestations in normal and glaucomatous eyes," *Exp. Eye Res.* **92**(5), 318–327 (2011).
7. L. Kagemann, G. Wollstein, H. Ishikawa, I. A. Sigal, L. S. Folio, J. Xu, H. Gong, and J. S. Schuman, "3D visualization of aqueous humor outflow structures in-situ in humans," *Exp. Eye Res.* in press.
8. M. Müller, H. Hörauf, G. Geerling, S. Pape, C. Winter, G. Hüttmann, R. Birngruber, and H. Laqua, "Filtering bleb evaluation with slit-lamp-adapted 1310-nm optical coherence tomography," *Curr. Eye Res.* **31**(11), 909–915 (2006).
9. C. K. Leung, D. W. Yick, Y. Y. Kwong, F. C. Li, D. Y. Leung, S. Mohamed, C. C. Tham, C. Chung-chai, and D. S. Lam, "Analysis of bleb morphology after trabeculectomy with Visante anterior segment optical coherence tomography," *Br. J. Ophthalmol.* **91**(3), 340–344 (2007).
10. M. Singh, T. Aung, M. C. Aquino, and P. T. Chew, "Utility of bleb imaging with anterior segment optical coherence tomography in clinical decision-making after trabeculectomy," *J. Glaucoma* **18**(6), 492–495 (2009).

11. K. Hirooka, M. Takagishi, T. Baba, and F. Shiraga, "Correlation between optical coherence tomography scan and histological specimen of a filtering bleb," *Acta Ophthalmol. (Copenh.)* **88**(2), e50–e51 (2010).
12. J. Ren, H. K. Gille, J. Wu, and C. Yang, "Ex vivo optical coherence tomography imaging of collector channels with a scanning endoscopic probe," *Invest. Ophthalmol. Vis. Sci.* **52**(7), 3921–3925 (2011).
13. Y. Fernández-Barrientos, J. García-Feijoó, J. M. Martínez-de-la-Casa, L. E. Pablo, C. Fernández-Pérez, and J. García Sánchez, "Fluorophotometric study of the effect of the glaukos trabecular microbypass stent on aqueous humor dynamics," *Invest. Ophthalmol. Vis. Sci.* **51**(7), 3327–3332 (2010).
14. M. C. Griehaber, A. Pienaar, J. Olivier, and R. Stegmann, "Canaloplasty for primary open-angle glaucoma: long-term outcome," *Br. J. Ophthalmol.* **94**(11), 1478–1482 (2010).
15. M. C. Griehaber, A. Pienaar, J. Olivier, and R. Stegmann, "Clinical evaluation of the aqueous outflow system in primary open-angle glaucoma for canaloplasty," *Invest. Ophthalmol. Vis. Sci.* **51**(3), 1498–1504 (2010).
16. J. A. McWhae and A. C. Crichton, "The use of ultrasound biomicroscopy following trabeculectomy," *Can. J. Ophthalmol.* **31**(4), 187–191 (1996).
17. J. M. Liebmann, "Ultrasound biomicroscopy of the anterior segment," *J. Glaucoma* **10**(5 Suppl 1), S53–S55 (2001).
18. A. Kobayashi and K. Sugiyama, "In vivo corneal confocal microscopic findings of palisades of Vogt and its underlying limbal stroma," *Cornea* **24**(4), 435–437 (2005).
19. D. V. Patel, T. Sherwin, and C. N. McGhee, "Laser scanning in vivo confocal microscopy of the normal human corneoscleral limbus," *Invest. Ophthalmol. Vis. Sci.* **47**(7), 2823–2827 (2006).
20. J. A. Izatt, M. R. Hee, E. A. Swanson, C. P. Lin, D. Huang, J. S. Schuman, C. A. Puliafito, and J. G. Fujimoto, "Micrometer-scale resolution imaging of the anterior eye in vivo with optical coherence tomography," *Arch. Ophthalmol.* **112**(12), 1584–1589 (1994).
21. S. Radhakrishnan, A. M. Rollins, J. E. Roth, S. Yazdanfar, V. Westphal, D. S. Bardenstein, and J. A. Izatt, "Real-time optical coherence tomography of the anterior segment at 1310 nm," *Arch. Ophthalmol.* **119**(8), 1179–1185 (2001).
22. S. Asrani, M. Sarunic, C. Santiago, and J. Izatt, "Detailed visualization of the anterior segment using fourier-domain optical coherence tomography," *Arch. Ophthalmol.* **126**(6), 765–771 (2008).
23. L. Kagemann, G. Wollstein, H. Ishikawa, R. A. Bilonick, P. M. Brennen, L. S. Folio, M. L. Gabriele, and J. S. Schuman, "Identification and assessment of Schlemm's canal by spectral-domain optical coherence tomography," *Invest. Ophthalmol. Vis. Sci.* **51**(8), 4054–4059 (2010).
24. K. Bizheva, N. Hutchings, L. Sorbara, A. A. Moayed, and T. Simpson, "In vivo volumetric imaging of the human corneo-scleral limbus with spectral domain OCT," *Biomed. Opt. Express* **2**(7), 1794–1802 (2011).
25. A. Tao, J. Wang, Q. Chen, M. Shen, F. Lu, S. R. Dubovy, and M. A. Shousha, "Topographic thickness of Bowman's layer determined by ultra-high resolution spectral domain-optical coherence tomography," *Invest. Ophthalmol. Vis. Sci.* **52**(6), 3901–3907 (2011).
26. Y. Yasuno, M. Yamanari, K. Kawana, M. Miura, S. Fukuda, S. Makita, S. Sakai, and T. Oshika, "Visibility of trabecular meshwork by standard and polarization-sensitive optical coherence tomography," *J. Biomed. Opt.* **15**(6), 061705 (2010).
27. G. Savini, M. Zanini, and P. Barboni, "Filtering blebs imaging by optical coherence tomography," *Clin. Exp. Ophthalmol.* **33**(5), 483–489 (2005).
28. R. K. Wang and L. An, "Multifunctional imaging of human retina and choroid with 1050-nm spectral domain optical coherence tomography at 92-kHz line scan rate," *J. Biomed. Opt.* **16**(5), 050503 (2011).
29. R. K. Wang, L. An, P. Francis, and D. J. Wilson, "Depth-resolved imaging of capillary networks in retina and choroid using ultrahigh sensitive optical microangiography," *Opt. Lett.* **35**(9), 1467–1469 (2010).
30. R. K. Wang, S. L. Jacques, Z. Ma, S. Hurst, S. R. Hanson, and A. Gruber, "Three dimensional optical angiography," *Opt. Express* **15**(7), 4083–4097 (2007).
31. R. K. Wang and S. Hurst, "Mapping of cerebro-vascular blood perfusion in mice with skin and skull intact by Optical Micro-AngioGraphy at 1.3  $\mu\text{m}$  wavelength," *Opt. Express* **15**(18), 11402–11412 (2007).
32. A. N. S. Institute, *American National Standard for Safe Use of Lasers: ANSI Z136.1–2000* (Laser Institute of America, 2000).
33. S. Ortiz, D. Siedlecki, I. Grulkowski, L. Remon, D. Pascual, M. Wojtkowski, and S. Marcos, "Optical distortion correction in optical coherence tomography for quantitative ocular anterior segment by three-dimensional imaging," *Opt. Express* **18**(3), 2782–2796 (2010).
34. A. Podoleanu, I. Charalambous, L. Plesea, A. Dogariu, and R. Rosen, "Correction of distortions in optical coherence tomography imaging of the eye," *Phys. Med. Biol.* **49**(7), 1277–1294 (2004).
35. V. Westphal, A. Rollins, S. Radhakrishnan, and J. Izatt, "Correction of geometric and refractive image distortions in optical coherence tomography applying Fermat's principle," *Opt. Express* **10**(9), 397–404 (2002).
36. D. J. J. Park and J. W. Karesh, *Topographic Anatomy of the Eye: an Overview*, Duane's Clinical Ophthalmology on CD-ROM (Lippincott Williams & Wilkins, 2006).
37. C. K. Leung and R. N. Weinreb, "Anterior chamber angle imaging with optical coherence tomography," *Eye (Lond.)* **25**(3), 261–267 (2011).
38. M. Doors, T. T. Berendschot, J. de Brabander, C. A. Webers, and R. M. Nuijts, "Value of optical coherence tomography for anterior segment surgery," *J. Cataract Refract. Surg.* **36**(7), 1213–1229 (2010).
39. S. Radhakrishnan, J. See, S. D. Smith, W. P. Nolan, Z. Ce, D. S. Friedman, D. Huang, Y. Li, T. Aung, and P. T. Chew, "Reproducibility of anterior chamber angle measurements obtained with anterior segment optical coherence tomography," *Invest. Ophthalmol. Vis. Sci.* **48**(8), 3683–3688 (2007).

## 1. Introduction

The corneo-scleral limbus is a transitional zone in the anterior region of the eye and contains several significant biological components which are important to fundamental research and clinical management [1]. The corneal region includes the corneal arcades, an important area for nutrient supply and waste removal from the avascular cornea [1,2]. The same region contains the palisades of Vogt, considered to be both a repository of stem cells responsible for the maintenance of the corneal epithelium and to serve as a “barrier” for the conjunctival epithelial cells that prevents them from migrating to the corneal surface [3,4]. The scleral region contains a rich vascular distribution (conjunctival vessels, episcleral vessels, and intrascleral vessels), a vasculature responsible for supplying oxygen and nutrition to the limbal area [1,2,5]. The limbal area also contains the aqueous outflow system (including the trabecular meshwork, Schlemm’s canal, the aqueous and the episcleral veins), an important pathway that allows the aqueous humor to leave the eye and return to the vascular system [1,6,7]. Blockage of the outflow system disrupts the balance between the rate of aqueous production and drainage, consequently leading to an elevated intraocular pressure (IOP) followed by damage to the optic nerve resulting in glaucoma [6,7]. Additionally, surgeries that treat glaucoma are performed in the limbal area. For example, trabeculectomy results in filtering blebs that are prone to vascularization and thickening associated with fibrosis, issues amenable to assessment and treatment guidance through use of anterior segment optical coherence tomography (AS-OCT) [8–11]. Newer Schlemm’s canal surgery involves insertion of stents into the canal to bypass the trabecular meshwork [12,13]; proper placement of stents in relation to Schlemm’s canal collector channel ostia is likely to be important to success of the procedures. Canaloplasty involves tightening of a suture placed circumferentially in Schlemm’s canal to increase aqueous outflow. The status of Schlemm’s canal tissues is thought to be a major prognostic factor in success and may determine whether to consider such surgery [14,15]. Better imaging capabilities should provide the ability to make better surgical decisions in this area.

Currently, there are several methods that can image the anterior segment of the eye, such as gonioscopy, ultrasound biomicroscopy (UBM) and confocal microscopy. Gonioscopy is the current gold standard for the assessment of the anterior chamber angle configuration and is widely used in the diagnosis of primary angle-closure glaucoma. Ultrasound biomicroscopy (UBM) is capable of direct visualization of anterior chamber angle, and high frequency UBM provides high-resolution (~25 $\mu$ m axially and 50 $\mu$ m laterally) images of the internal microstructures of the anterior chamber of the eye with an imaging depth of ~5mm, which is suitable to characterize filtering blebs after trabeculectomy [16] and also provides information for postsurgical management [17]. Confocal microscopy, which provides cellular level resolution, has previously been used to image the structure of the limbus *in vivo*, including the palisades of Vogt [18,19]. Unfortunately, these techniques require contact with the eye and are less practical because they can cause discomfort, as well as carrying the risk of contact abrasions and infections. Furthermore, some of these examinations are highly subjective and depend on the experience of the examiner. Therefore, there is a need to develop a method capable of non-invasively imaging the three-dimensional microstructure and microvasculature of the corneo-scleral limbus, including the aqueous outflow system.

Optical coherence tomography (OCT) is a powerful noncontact, noninvasive, real-time imaging modality with high spatial resolution (< 20 $\mu$ m axially). Significant developments have been achieved in ocular imaging using AS-OCT [7,13–20], since its first demonstration [20]. The imaging depth of AS-OCT has been enhanced by using a longer wavelength of light (~1300nm) [21], where the tissue presents low scattering properties. Fourier domain OCT (FD-OCT), including swept source OCT (SS-OCT) and spectral domain OCT (SD-OCT), has significantly increased the imaging speed and minimized the motion artifacts [7,22–25]. The use of new broadband light sources enables the AS-OCT to increase the imaging axial resolution (<10 $\mu$ m) [7,22,24]. Also, new contrast mechanisms, such as Doppler OCT and

polarization-sensitive OCT (PS-OCT), have been used to enhance the image visibility of several ocular structures, such as the trabecular meshwork [23,26].

Recent studies have revealed the potential of using OCT for corneo-scleral limbus imaging [7–11,22–24,26,27]. Kagemann *et al.* measured the regional variation in cross-sectional areas of the human Schlemm's canal based on an ultrahigh resolution SD-OCT imaging system (1.3 $\mu$ m theoretical axial resolution, operating at 870nm) [23]. In their following study, Kagemann *et al.* presented a 3D *in vitro* visualization of the aqueous outflow system [7]. Recently, Bizheva reported the *in vivo* 3D structural details from the palisades of Vogt, the blood and lymph vasculature, Schlemm's canal and the trabecular meshwork (TM) in the limbal area using an ultrahigh resolution (3 $\mu$ m axially and 18 $\mu$ m laterally) SD-OCT operating at 1020nm [24]. However, the use of scattering-based OCT to observe the blood vessels from the structural en-face OCT images proved to be problematic because the scattering background from the adjacent tissue would often mask the ability to segment the blood vessels. Also, it is hard to differentiate the blood vessels from the lymph vessels. Additionally, several studies have shown that, AS-OCT would be suitable for postsurgical management of glaucoma, due to its non-contact, non-invasiveness and high resolution [8–11,27].

In this study, we employed a laboratory-built AS-OCT system based on a SD-OCT configuration with a 1300nm band light source, to provide high penetration depths, allowing image acquisition of the human corneo-scleral limbal area *in vivo*. The optical microangiography (OMAG) algorithm was employed to extract the microstructural and microvascular images in parallel [28–31]. The aqueous outflow pathway was mapped by analyzing the obtained microstructural and microvascular information. To our knowledge, this is the first demonstration of using a SD-OCT system to noninvasively obtain the 3D information about the microcirculation and aqueous outflow pathway *in vivo* from the corneo-scleral limbus.

## 2. Material and methods

An AS-OCT system based on the SD-OCT configuration has been developed. As shown in Fig. 1, the system contains a broadband superluminescent diode (SLD, DenseLight, Singapore) with a central wavelength of 1310nm and a spectral bandwidth of 60nm which is used as a low coherence light source. The axial imaging resolution is ~12 $\mu$ m in air. The emitted radiation from the SLD is coupled into a fiber-optic Michelson interferometer via a circulator, and then equally split into the sample and reference arm by a 50/50 optical coupler. In the sample arm, the light is focused by an objective lens with a focal length of 75 mm, yielding a measured lateral resolution of ~44 $\mu$ m. The light reflected from both the sample and the reference mirror is recombined in the optical coupler, and the resulting interference signal is directed to a laboratory-built spectrometer through the circulator. The spectrometer is equipped with an InGaAs line scan camera (SU1024LDH2, Goodrich Ltd. USA), capable of ~92 kHz A-line scan rate. The spectrometer has a spectral resolution of 0.14 nm providing a measured imaging depth of ~3.0 mm in air, and has ~102dB sensitivity around the zero-delay line and ~14dB roll-off from 0.5mm to 2.5mm imaging-depth position. A measured light power of ~2mW is exposed on the sample, which is within the American National Standards Institute safety limit [32].

The scanning protocol was optimized to implement the OMAG algorithm [28–31]. In the fast-scan direction (i.e., B-scan), it contained 360 A-lines that covered ~5.5 mm. With this configuration, the B-scan frame rate of the system was ~200 frames per second. In the slow-scan direction (i.e., C-scan), 200 sampling positions, covering ~4 mm distance, were used to capture one 3D data set, with five repeated B-frames at every position. The five repeated B-frames were used for the OMAG calculation, and the results of which were averaged to obtain both the structure and blood flow images. Therefore, 1000 B-scans were acquired to form a 3D data cube, corresponding to an acquisition time of ~5 seconds. The experiment was conducted *in vivo* in the corneo-scleral region of a healthy human subject, which was approved by the Institutional Review Board at the University of Washington.

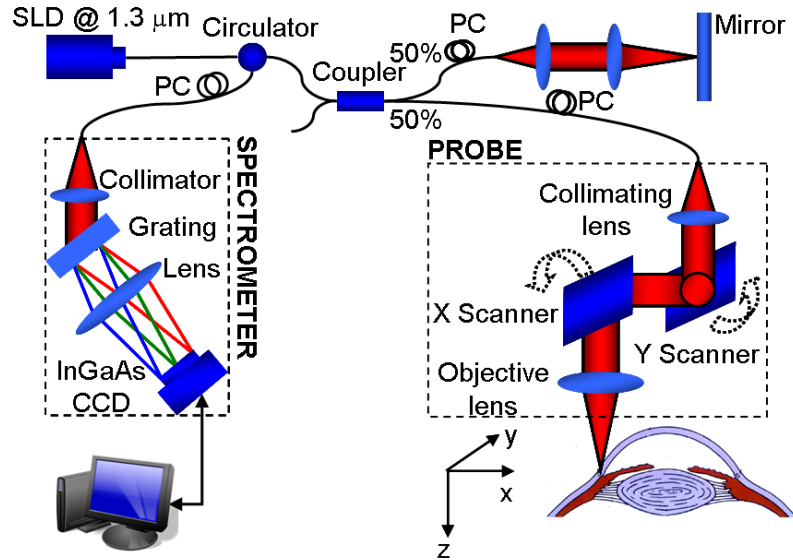


Fig. 1. Schematic diagram of the AS-OCT system.

Once the acquisition of the OCT data set was completed, the OMAG algorithm was applied to the data set in order to extract the microstructural and microvascular images in parallel [28–31]. OMAG is largely based on the Doppler phase shift due to the moving particles, and to a lesser extent, on the dynamic speckle between B-frames; therefore, it is able to effectively separate the light scattering due to the moving particles from that due to the static tissue bed [30,31]. However, in the microstructural images, due to the non-telecentric scan, i.e. the fan scan pattern, and the refraction of the probing light beam, the physical geometry of the anterior chamber was distorted [33–35]. In order to quantitatively determine the anterior chamber biometry, an algorithm based on Fermat's principle was used to correct the optical distortions [35].

### 3. Results

#### 3.1 Microstructural imaging

The microstructural images obtained with the AS-OCT system, allow for the identification of several biological components. Figure 2(A) shows a schematic diagram of the microstructural components in the limbal area (modified from [36]), and Fig. 2(B) shows a representative OCT structural cross-section of the human corneo-scleral limbus acquired from a temporal location. In the corneal region, the corneal epithelium (CnE) and the corneal stroma (CnS) can be identified. In the limbal area, between the cornea and the conjunctiva and sclera, the CnE transits into the bulbar conjunctival epithelium (CjE). The CjE appears more optically opaque compared to the CnE. Beneath the CjE, there is a relatively weak scattering layer, the conjunctival stroma (CjS), where the first layer of vasculature is located (see Fig. 3(B) and 3(C)) [1]. Below the CjS is the episclera (ES) where large blood vessels are located [1]. The iris (I) and the ciliary body (CB) appearing as a dark area at the root of the iris can be observed. The strong scattering area between the CB and ES corresponds to the sclera (S). The scleral spur (SS) which is an important landmark in determining the anterior angle, is also visible. Due to the limited spatial resolution of the system, the Bowman's layer and Descemet's membrane, which is used to define the histologic limit of corneal limbus [1], is not clearly visible. Also, the trabecular meshwork (TM) and Schlemm's canal (SC) are difficult to discern in the current structural image.

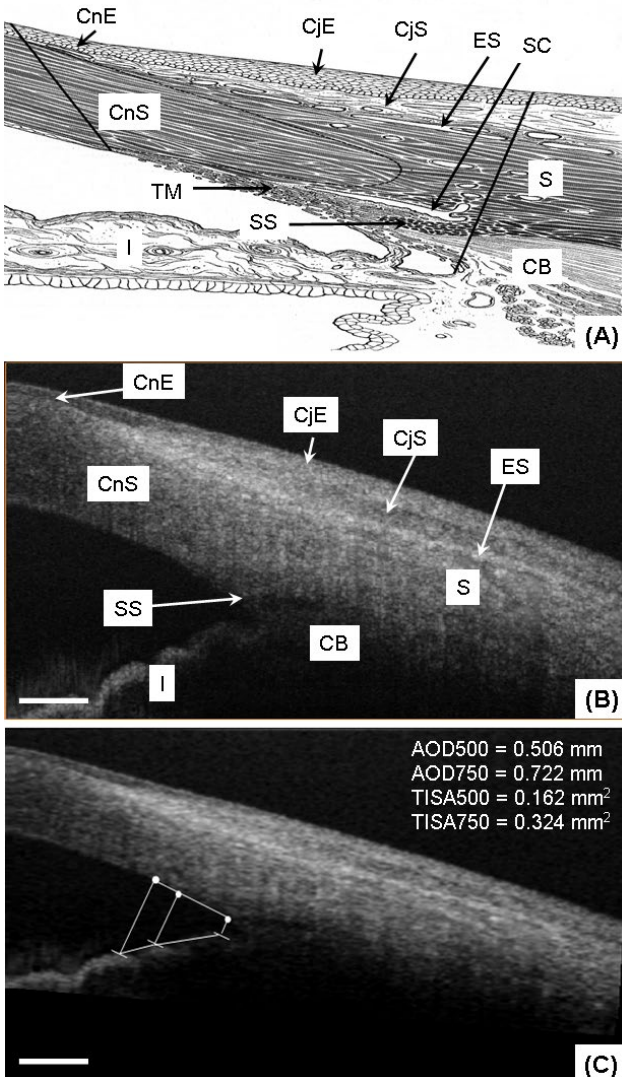


Fig. 2. *In vivo* microstructure imaging of the human corneo-scleral limbus from a temporal location. (A) Schematic diagram of the microstructure in the limbal area (modified from [36]); (B) A representative OCT structural cross-section consisting of 360 A scans covering ~5.5mm; (C) The same cross-section after the correction of the optical distortions. AOD and TISA measurements are included. CnE: corneal epithelium; CnS: corneal stroma; CjE: conjunctival epithelium; CjS: conjunctival stroma; ES: episclera; S: sclera; SS: scleral spur; CB: ciliary body; I: iris; TM: trabecular meshwork. The scale bar represents 600 $\mu$ m.

The microstructural images can be used to quantitatively assess anterior chamber biometry [37–39]. Figure 2(C) presents the anterior chamber angle configuration after the correction of the non-telecentric and refraction distortion. Considerable changes between Figs. 2(B) and 2(C) can be observed in the width of the cornea and the anterior chamber angle, which can be primarily ascribed to the refraction distortion. Because, in addition to the relative small scan range, a long focal length (~75mm) of the objective lens was used in this study, the non-telecentric distortion is not obvious in this AS-OCT. According to [37–39], the angle opening distance (AOD) and the trabecular-iris space area (TISA) measurements were obtained and reported in the figure as a demonstration of its applicability for biometric measurements.

### 3.2 Microvascular imaging

The blood supply of the limbus area originates from the anterior ciliary artery (ACA) which divides to form the conjunctival plexus (CP), the episcleral plexus (EP) and the intrascleral plexus (IP) [1,2]. Figure 3(A) (modified from [36]) shows a schematic diagram of the blood supply to the limbus area. Figure 3(B), presents a cross-sectional blood flow image obtained using the OMAG algorithm. In this image we can identify the CP, EP and IP regions. Figure 3(C) is a superposition of the microstructural and microvascular image to better illustrate the spatial location of the blood flow.

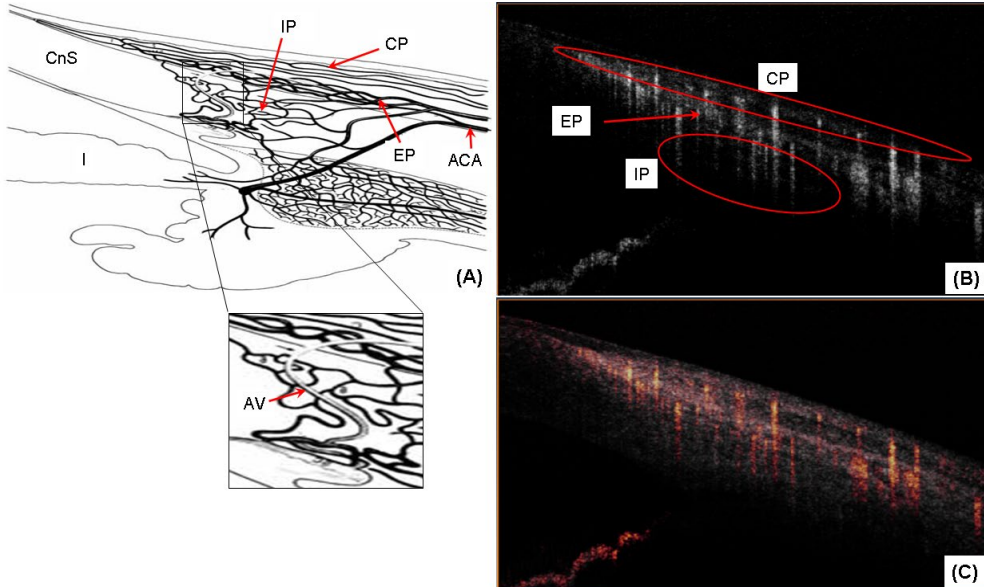


Fig. 3. *In vivo* microvasculature imaging of the human corneo-scleral limbus from a temporal location. (A) Schematic diagram of the blood supply in the limbal area. The enlarged part illustrates the aqueous vein (modified from [36]); (B) OMAG vascular cross-section corresponding to Fig. 2(B); (C) OMAG vascular cross-section superimposed with structural cross-section (Fig. 2 (B)). ACA: anterior ciliary artery; CP: conjunctival plexus; EP: episcleral plexus; IP: intrascleral plexus; AV: aqueous vein.

The three-dimensional depiction of the microvasculature can be observed in Fig. 4(A), and the projection view is presented in Fig. 4(B). A fraction of the CP is terminal vessels (TV) which reach the palisades of Vogt to supply the peripheral corneal arcades, observed in Fig. 4(B). Another part of the CP is recurrent vessels (RV), which run posteriorly to supply the perilimbal area, and is observed in Fig. 4(C) which is an oblique slice of the microvasculature across the conjunctival area. The RV presents a linear pattern with few interlacing vessels. The IP extend deep into the area around Schlemm's canal to supply the middle and deep sclera. Blood is collected by a fine venous network and transported out of the limbus via the episcleral veins. The blood vessels in the sclera form a compact reticular arrangement, observed in Fig. 4(D) which is an oblique slice across the scleral area. Additionally, the largest blood vessel, as indicated by the bold white arrow in Figs. 4(A), 4(B) and 4(D), most likely corresponds to an episcleral vein, which can be confirmed by the observation that this vessel is connected to Schlemm's canal via the aqueous vein (described in the following section).

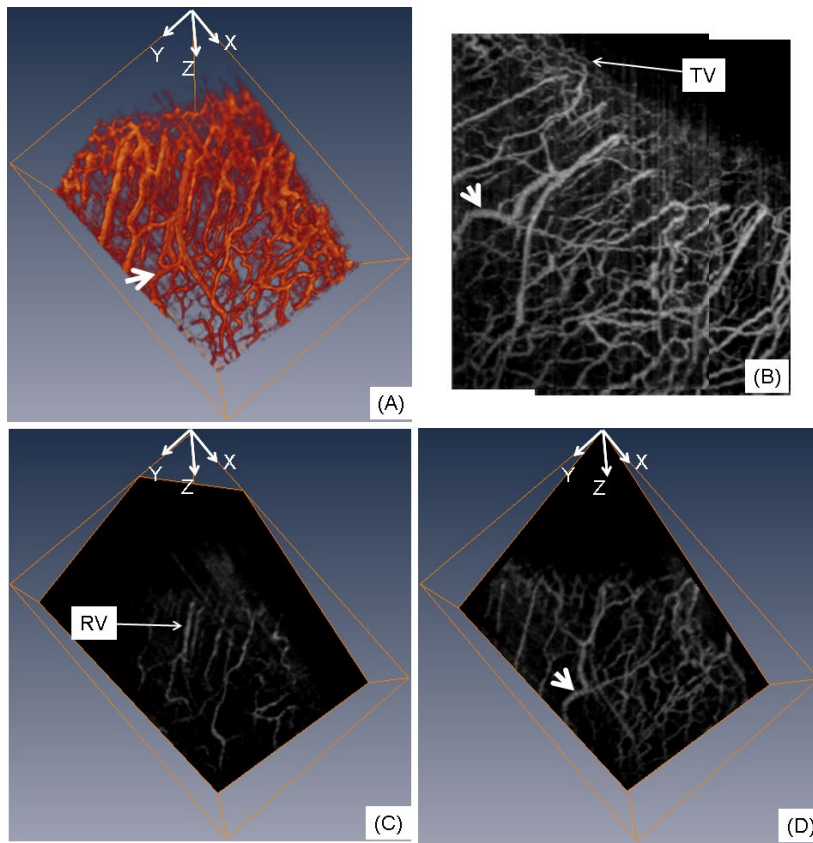


Fig. 4. *In vivo* 3D blood flow imaging of the human corneo-scleral limbus from a temporal location. (A) 3D rendering of the flow images; (B) projection view (x-y) from the 3D blood flow image; (C) oblique slice of (A) within the conjunctival layer; (D) oblique slice of (A) in the scleral area. Bold white arrow indicates the episcleral vein; TV: terminal vessel; RV: recurrent vessel. The physical image size was  $5.5 \times 4.0 \times 3.0$  (x-y-z) mm<sup>3</sup>.

### 3.3 Aqueous outflow pathway mapping

The aqueous humor is a transparent water-like fluid filling the space between the lens and the cornea. The aqueous humor exits the eye through the aqueous outflow pathway, which contains the trabecular meshwork, Schlemm's canal, the aqueous and the episcleral veins. If the pathway is blocked or not working normally, aqueous humor will not properly drain from the eye. Blockage causes an increase in intraocular pressure which may lead to glaucoma. Figure 5 shows the cross-sectional structural images indicating the traces of aqueous humor pathway, such as aqueous vein (Figs. 5(A)–5(D)), and episcleral vein (Figs. 5(E), 5(G)). In Figs. 5(A)–5(D), the flow travels from the area around Schlemm's canal to the episcleral vein (Figs. 5(E), 5(F) and 5(H)) confirm that the destination of the flow is the episcleral vein. The weak signal regions in Figs. 5(A)–5(D), as shown by the thin arrows, can be mainly attributed to the transparent aqueous flow in the aqueous vein. Additionally, the shadow below the flow demonstrates the appearance of the moving blood accompanying the aqueous flow in the aqueous vein. By making use of this characteristic, the 3D aqueous vein can be segmented out from the stronger signal of the structures surrounding the aqueous veins. Combining the 3D information of the episcleral vein, which can be obtained from Fig. 4(A), and the aqueous vein, obtained from the structural images, we were able to obtain the 3D aqueous outflow pathway, as shown in Fig. 6 (Refer to the enlarged part of Fig. 3(A)).

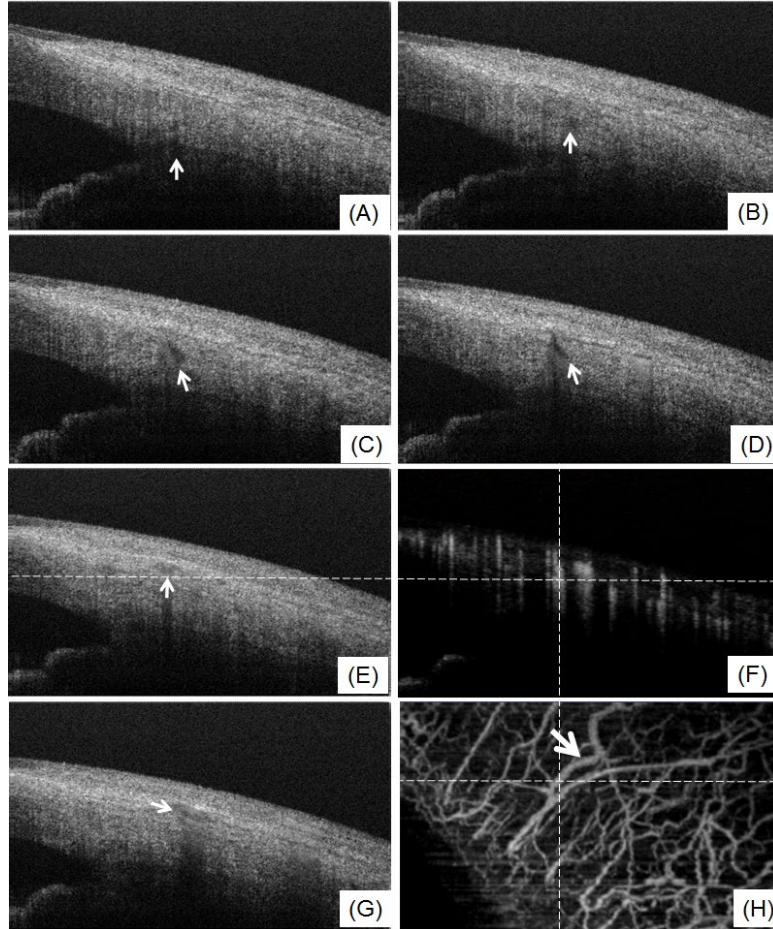


Fig. 5. (A-E and G) Selected structural cross-section showing the traces of aqueous outflow pathway from aqueous vein (A-D) to episcleral vein (E, G); (F) OMAG blood flow cross-section corresponding to (E); (H) projection view of blood flow image and the lateral dash line corresponds to the position of (E) and (F). (F) and (H) indicate that the destination of the flow is the episcleral vein. Bold white arrow indicates the episcleral vein.

#### 4. Discussion

This study demonstrated that the AS-OCT can obtain 3D microstructural and microvascular images of the anterior chamber of the eye in parallel, without the use of exogenous contrast agents, by using an OMAG algorithm. The microstructural images enable the visualization of several tissue layers and structures. After applying the numerical correction of the optical distortions, it is possible to quantify several biometric parameters, such as the AOD and TISA. The microvascular images allow the identification of several vessel patterns, including the episcleral veins distribution. By combining the structural and vascular information it is possible to extract the microcirculation located within different tissue layers and structures, and to map the aqueous outflow pathway from *in vivo* human subjects.

However, some limitations are present in the currently configured AS-OCT system. As discussed by Kagemann *et al.* [23], the shadows from the superficial blood vessels significantly influence the image quality, specifically the resolution of the blood flow images at increasing depths, which can be improved by increasing the axial resolution. Also, increasing the axial resolution of the current system would help to visualize the entire outflow

pathway, such as the trabecular meshwork and Schlemm's canal, as well as to obtain more detailed information related to the palisades of Vogt and thin layers like the cornea tear film.

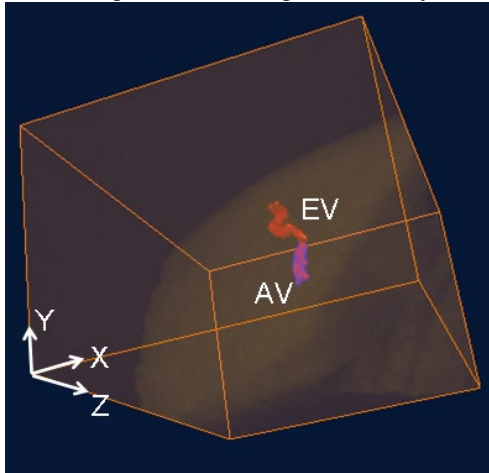


Fig. 6. Volumetric rendering of the merged 3D micro-structure and aqueous outflow pathway (aqueous vein and episcleral vein). EV: episcleral vein; AV: aqueous vein.

The blindness caused by glaucoma is irreversible and is usually recognized when the disease has significantly progressed as manifested by optic nerve cupping or field loss. Early diagnosis is important to slow or stop the progression of the development of glaucoma. The only treatable risk factor in glaucoma is pressure, and abnormalities of pressure control reside in the aqueous outflow system. Thus, early recognition of abnormalities of the aqueous outflow system may permit earlier identification and management of the one treatable risk factor in the optic neuropathy of glaucoma. For the assessment of primary angle-closure glaucoma, the anterior chamber angle configuration and status of structures within the aqueous outflow system can be concurrently monitored to permit more informed decisions concerning management.

Usually, glaucoma is surgically treated via a trabeculectomy, thus creating filtering blebs, which develop neovascularization and fibrotic thickening [8–11,27]. Because AS-OCT is a noncontact technique it can be used preoperatively to assess the health of the conjunctiva and postoperatively to simultaneously monitor fibrotic thickening and neovascularization, issues important to decision making in postsurgical management.

Other applications for the AS-OCT include the study of the microcirculation in the corneal arcades and palisade of Vogt, to better identify issues and assess the effects of treatment in conjunctival and corneal diseases.

## 5. Conclusion

The integration of the AS-OCT with the OMAG method has enabled us to demonstrate an application for imaging both the microstructure and microvasculature of the corneo-scleral limbus in an *in vivo* human eye. Using these images we have also been able to map the aqueous outflow pathway and limbal vasculature. The results indicate the potential for further development of the AS-OCT as a useful tool for studying the corneo-scleral limbus, and we expect it to have future applications in the diagnosis, monitoring and treatment of glaucoma.